PAPER

Check for updates

Fabrication of an In₂O₃ NP-based high-performance low-operating voltage phototransistor and tuning of its photosensitivity from UV to blue region†

Akhilesh Kumar Yadav,[a] Utkarsh Pandey, [ID][a] Pijush Kanti Aich,[a] Vishwas Acharya,[a] Swati Suman[b] and Bhola N. Pal [ID] *[a]

In this work, a visible-blind low-operating voltage phototransistor was fabricated using colloidal In₂O₃ nanoparticles (NPs) *via* a solution process technique, and its photosensitivity was tuned to the blue region by adding a PbI₂ layer to the channel. The low-voltage operation of this thin-film transistor (TFT) was achieved by employing an LiInSnO₄ gate dielectric with high areal capacitance, which originated from the mobile Li⁺ ions inside the dielectric thin film. Furthermore, the photosensitivity of the low-voltage TFT was improved through the implementation of an asymmetric source–drain (S–D) electrode of TFT with different work functions, which worked as a driving voltage for photo-generated carriers. Specifically, LiF/Al and MoO₃/Ag were used as source and drain electrodes, respectively, which exhibited a work-function difference of ∼−1.16 eV. Incorporating these asymmetric S–D electrodes markedly improved the performance of the In₂O₃ NP TFT, reducing the subthreshold swing (SS) from 682 to 160 mV per decade, representing a fourfold decrease, and enhancing the on/off current ratio by an order of magnitude. As the band gap of In₂O₃ NP was ∼3.7 eV, the device was sensitive only towards deep UV region, making it a visible-blind device. The photosensitivity of the device under UV illumination was enhanced by twenty times using the asymmetric S–D electrodes. The photo-response band of this TFT was further tuned to the blue region by adding a PbI₂ layer on the In₂O₃ channel of the TFT. The photosensitivity of the asymmetric electrode-based PbI₂/In₂O₃ heterojunction TFT in the deep UV (∼395 nm) and blue (∼445 nm) regions was 492 and 152, respectively.

1. Introduction

In the last two decades, a large variety of photodetector (PD) devices have been reported owing to their various applications in image sensing, optical fiber communication, wireless communication, and bio-medical applications.[1,2] These PDs are made up of various materials, including different conventional semiconductors, inorganic nanostructure materials, metal oxide semiconductors, and organic semiconductors, with different device structures such as photoconductors, photodiodes and phototransistors.[3–5] Among these devices, photo-transistors have various advantages including their high gain with excellent sensitivity.[6,7] Besides, the semiconductor channel of a phototransistor can be directly illuminated with an optical signal that can avoid loss of optical signal, making them highly suitable for low-light detection and imaging applications. This is serious concern particularly for UV- and blue-sensitive photodetectors because of their poor penetration depth.[8–10] Moreover, during photocurrent generation of a phototransistor, multiple device parameters change, enabling one to pick up the most sensitive parameter to calibrate the device with light intensity.[8,11]

Among the various semiconductors, Si is the most widely used material for photodetector application because of its unique band gap of 1.1 eV that facilitates fabricating a device which is sensitive from the UV to the NIR region. Moreover, the synthesis method of Si is a highly advanced one, which enables growing highly crystalline Si with extremely high purity. Si can be doped either with p- or n-type dopants, which commonly require tuning of its charge transport properties in different microelectronics and optoelectronics applications. However, the Si PD exhibit poor response to the UV and blue

[a] School of Materials Science and Technology, Indian Institute of Technology (Banaras Hindu University), Varanasi-221005, India. E-mail: bnpal.mst@iitbhu.ac.in
[b] Electronic Materials and Thin Films Lab, Department of Metallurgical and Materials Engineering, Indian Institute of Technology (IIT) Madras, Chennai, India
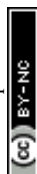
regions for its indirect semiconducting nature, which requires at least several tens of micrometer widths to absorb photons efficiently.[12] However, UV and blue light have a poor penetration depth to the crystalline Si. Therefore, for UV/blue photodetector fabrication, wide band gap semiconductors such as SiC, GaN, halide perovskite, and metal oxide semiconductors are widely used.[13–17] Among them, metal oxide semiconductors are also commonly used for the fabrication of n-channel TFTs because of their high electron mobility, and easy and low cost fabrication method.[18–21] Again, the fabrication of these TFTs using a high-κ dielectric can reduce the operating voltage of the TFT, which is required for portable PDs.[22–24] However, UV/blue responsivity and detectivity of these devices need to be improved with more cost-effective fabrication techniques for their realistic applications.

In this work, a low-voltage In_2O_3 nanoparticle (NP)-based phototransistor was fabricated using an ion-conducting $LiInSnO_4$ dielectric via a solution process. The performance of the TFT was improved by employing an asymmetric work function source–drain (S–D) electrode. These two different electrode combinations were chosen to collect photo-generated electrons and holes selectively from the semiconductor channel to the electrodes at a faster rate. Additionally, an $LiInSnO_4$ thin film was used as a gate insulator that has high areal capacitance due to the mobile Li^+ ions inside the dielectric thin film, which can reduce the operating voltage of these TFTs to 2.0 V.[25] This asymmetric S–D electrode In_2O_3 NP TFT exhibited a substantial improvement in the on/off ratio and subthreshold swing reduction. Importantly, ~two order of improvement of photosensitivity of the device was observed with respect to the symmetric electrode TFT, which is a very necessary requirement to overcome the limitations of earlier efforts on UV/blue photodetector works.[13,26] This improvement was attributed to the selective and efficient collection of electrons and holes by the electrodes, driven by their work function difference of the S–D electrodes. The photosensitivity of this TFT is restricted only in the UV region due to the wide band gap of In_2O_3 NP, making it a visible-blind UV photodetector.[27] Further, a PbI_2 layer was added on the channel of this TFT to tune the photo-response band of the device from the UV to the blue region without reducing its device performance.

2. Experimental section

2.1. Material synthesis

The synthesis of the precursor solution for $LiInSnO_4$ thin films involved the equimolar integration of lithium acetate $[C_2H_3LiO_2]$ (purity > 98.0%, TCI), anhydrous indium chloride $[InCl_3]$ (purity > 99.99%, Alfa Aesar), and tin(ii) chloride $[SnCl_2]$ (purity > 99.99%, SIGMA-ALDRICH). These three individual components are dissolved in 2-methoxy ethanol (2MEA) separately to prepare a solution of concentration 200 mM each via rigorous stirring for one hour under ambient conditions. Then these solutions are mixed in a volume ratio of 1/1/1 to prepare a 200 mM precursor solution for $LiInSnO_4$ (LITO). Further, this precursor solution was filtered through a PVDF syringe (0.45 μm) filter to remove

unwanted microparticles. For the semiconductor channel deposition, a commercial indium(iii) oxide nanoparticle (In_2O_3 nano powder <100 nm particle size, 99.99%, Sigma Aldrich) was dispersed in 2-methoxy ethanol (2MEA) in definite quantity and subjected to ultrasonic sonication. Lead(ii) iodide (PbI_2), purchased from Sigma Aldrich (99%), was dissolved in dimethyl formamide (DMF), to prepare a solution of concentration 5 mg ml^{-1}, which was used as an additional photosensitive layer to tune the photo-response of the TFT.

2.2. Device fabrication

The heavily p-doped silicon substrate (p^+-Si) with dimensions of 15 mm × 15 mm was used as a substrate and cleaned with an extran solution (MA02, Merck) to remove macroscopic contamination. Subsequently, the substrates were subjected to a wet cleaning process in an ultrasonic bath using DI water, acetone, and isopropyl alcohol for 20 minutes each in succession.[28] To abolish the effect of organic substances, the wet-cleaned substrates were treated with an oxygen plasma for 10 minutes. After cleaning, the precursor solution of $LiInSnO_4$ (200 mM) was spin-coated onto the substrates at 5000 rpm for 50 seconds, placed on a preheated hot plate at 90 °C for 5 minutes and subsequently transferred to a pre-heated (350 °C) furnace where it annealed for 30 minutes. This dielectric coating process was repeated three times followed by final annealing at 500 °C for 1 hour. Then the colloidal solution of In_2O_3 NPs is spin coated onto the dielectric film at a speed of 4000 rpm for 45 s followed by an ambient atmosphere annealing process at 125 °C for 30 minutes. The thickness of the prepared $LiInSnO_4$ and In_2O_3 tin films are 90 and 30 nm, respectively, which are also shown in the cross-sectional SEM data in the 'Surface morphology and thickness analysis' section. Finally, S–D electrodes with a 'width-to-length' ratio (W/L) of 118 (23.6 mm/0.2 mm) were deposited by a thermal evaporation method. Aluminum S–D electrodes were used for symmetric electrode devices (Device-1), whereas LiF (4.5 nm)/Al (60 nm) and MoO_3 (4.5 nm)/Ag (60 nm) were used as source and drain electrodes, respectively, for the asymmetric electrode device (Device-2). In case of asymmetric electrodes, LiF and MoO_3 were used as interface materials of Al and Ag electrodes, respectively.[29] After the electrical and optical characterization of these devices, the PbI_2 (Lead(ii) iodide) precursor solution was spin-coated on top of these TFTs at a speed of 2500 rpm for 1 minute, and subsequently, kept on the preheated hot-plate at 60 °C for 20 minutes to remove the solvent. Besides, a set of devices were fabricated on a p^+-Si substrate following exactly the same procedure by using an Al top electrode, but excluding the In_2O_3 layer (Al/$LiInSnO_4$/p^+-Si). This metal–insulator–metal (MIM) geometry device was used for the electrical characterization of the $LiInSnO_4$ dielectric thin film. The real and SEM images of Device-1 and Device-2 with labelled source (S), Drain (D) and Gate (G) electrodes are shown in Fig. SI 1.†

2.3. Material characterization

The structural examination of $LiInSnO_4$ and In_2O_3 NP thin films were carried out using an X-ray diffractometer (Rigaku)

with monochromatic Cu Kα radiation (λ = 0.15405 nm). An Atomic Force Microscope (AFM) (NT-MDT NTEGRA-prima) was used to investigate the surface morphology of various layers comprising the device structure. The UV–Visible spectrophotometer (JASCO V-650) assisted us in determining the absorption spectra of the semiconducting material, which was the focal point of this research. Capacitance *vs.* frequency (C–f) measurements of thin-film dielectric samples were carried out using an LCR meter (Keysight Technology Model E4990A). Electrical characterization of Thin-Film Transistors (TFTs) and leakage current measurements of the dielectric material were performed using a semiconductor parameter analyzer (Keysight B1500 A). The External Quantum efficiency (EQE%) data were investigated using a quantum efficiency measurement set-up (ENLITECH QE-R). Electrical connections with the devices were established using a micromanipulator of a manual probe station. All electrical measurements were conducted under open atmospheric conditions.

3. Results and discussion

3.1. Structural analysis of LiInSnO$_4$ and In$_2$O$_3$ NPs

The Grazing Incidence X-ray Diffraction (GIXRD) patterns of LiInSnO$_4$ and In$_2$O$_3$ NP thin films are shown in Fig. 1(a) and (b), respectively. In Fig. 1(a), no clear peaks are observed in the GIXRD pattern of the LiInSnO$_4$ dielectric thin film, revealing an amorphous phase of the film.[4] Fig. 1(b) shows the XRD data of In$_2$O$_3$ nanoparticles, indicating its diffraction peaks at 2θ angles of 20.9°, 30°, 34.8° and 50.4°, which correspond to the (112), (222), (400), and (440) reflection planes, respectively. The heightened intensity observed from the (222) plane serves as clear evidence of the cubic phase (JCPDS No. 06-0416) of the In$_2$O$_3$ NPs.[30,31]

3.2. Optical properties of LiInSnO$_4$ and In$_2$O$_3$ NPs

The optical properties of the LiInSnO$_4$ gate dielectric and In$_2$O$_3$ NPs thin films were analyzed using a UV-Vis spectrophotometer, and the results are shown in Fig. 2. For this optical study, the LiInSnO$_4$ thin film was deposited on a quartz substrate, which demonstrates an average transmittance above 85% in the visible
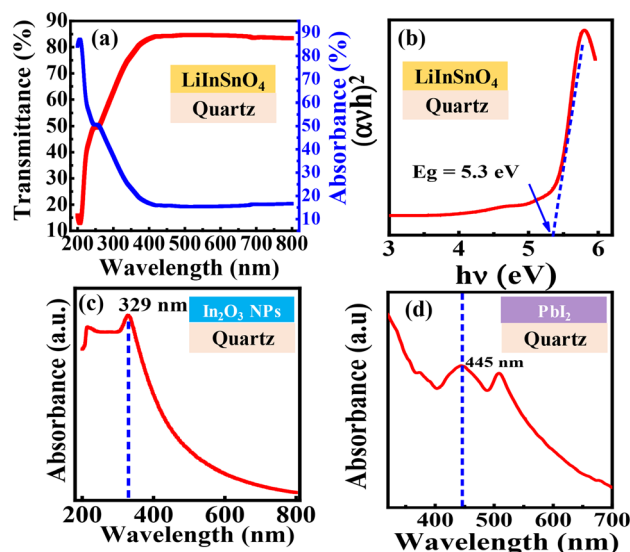
Fig. 1 (a) GIXRD pattern of LiInSnO$_4$ thin film, indicating its amorphous phase and (b) GIXRD pattern of In$_2$O$_3$ nanoparticles thin film, indicating the crystalline nature of the nanoparticle.

Fig. 2 (a) Optical transmittance/absorbance spectra of the solution-processed LiInSnO$_4$ dielectric thin film annealed at 550 °C for LiInSnO$_4$/quartz. (b) Tauc plot of LiInSnO$_4$; the band gap is 5.3 eV. Absorbance spectra of (c) In$_2$O$_3$ NPs and (d) PbI$_2$ thin films.

range (400–800 nm), indicating minimal impurities and defects (Fig. 2(a)). Besides, from Fig. 2(a), it is clear that the LiInSnO$_4$ thin film has absorption in the deep UV region only. Tauc plot of these absorption data reveals an optical band gap of 5.3 eV of the LiInSnO$_4$ thin film (Fig. 2(b)), which is suitable as the gate dielectric of a TFT. Similarly, UV-Vis measurements of an In$_2$O$_3$ thin film show an absorbance peak at 330 nm, (Fig. 2(c)). These findings indicate the optical band gap of In$_2$O$_3$ NPs to be ~3.75 eV. Additionally, the UV-Vis absorption spectra of the PbI$_2$ thin film on a quartz substrate are shown in Fig. 2(d), displaying a prominent peak across 445 nm wavelength, which can allow the device to respond under the blue region (445 nm) of the electromagnetic spectra.

3.3. Surface morphology and thickness analysis

The surface roughness of individual films plays a vital role in the device's performance. For this assessment, atomic force microscopic (AFM) study of the LiInSnO$_4$ and In$_2$O$_3$ NPs was performed. Fig. 3(a) and (b) show the 2D and 3D AFM images of the LiInSnO$_4$ thin film. The root mean square (RMS) surface roughness of this film is 0.29 nm, which is quite low for its use as a gate dielectric of a TFT.[32] In addition, the AFM analysis was also performed for the In$_2$O$_3$ NP-coated LiInSnO$_4$ dielectric thin film, *i.e.* on the surface of p$^+$-Si/LiInSnO$_4$/In$_2$O$_3$. The 2D and 3D AFM images of that surface are shown in Fig. 3(c) and (d), respectively, and indicate its RMS roughness of ~1.42 nm, which is quite low. For the thickness measurement of LiInSnO$_4$ and In$_2$O$_3$ NP thin films, a cross-sectional FESEM analysis of p$^+$-Si/LiInSnO$_4$/In$_2$O$_3$ was performed, and the image is shown in Fig. 3(e). The measured thickness of the LiInSnO$_4$ and In$_2$O$_3$ NP thin film, as obtained from this study, are 90 nm and 30 nm, respectively.
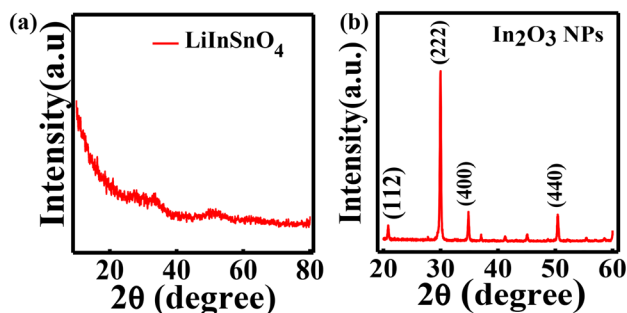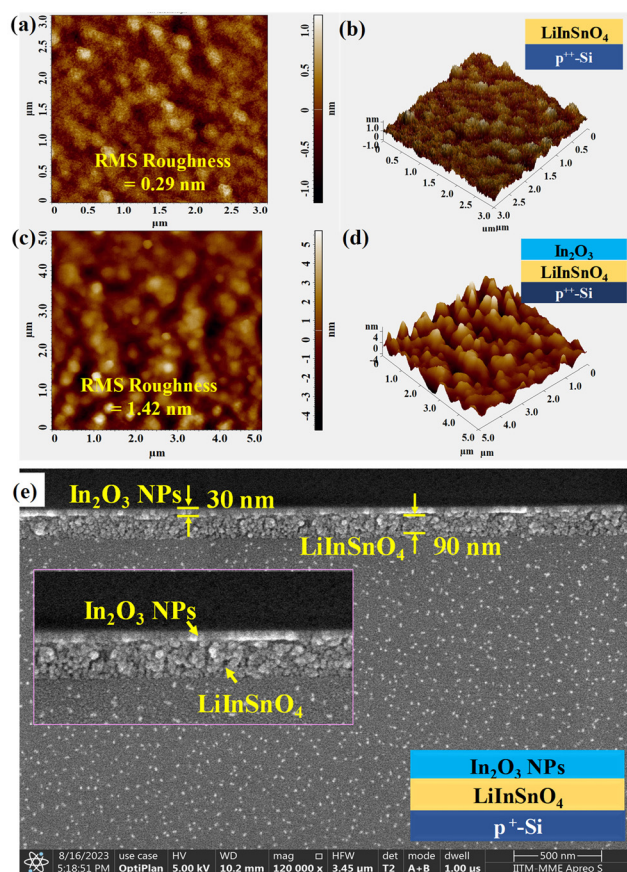
Fig. 3 AFM images: (a) 2D and (b) 3D images of LiInSnO$_4$ dielectric thin film (p$^+$-Si/LiInSnO$_4$) with R_{rms} ~ 0.29 nm, (c) 2D and (d) 3D images of In$_2$O$_3$ NPs thin film (p$^+$-Si/LiInSnO$_4$/In$_2$O$_3$) R_{rms} ~ 1.42 nm, and (e) cross-sectional SEM image of the p$^+$-Si/LiInSnO$_4$/In$_2$O$_3$ NP film.

### 3.4. Dielectric measurement of LiInSnO$_4$ through an MIM device

Capacitance *vs.* frequency (C–f) and current *vs.* voltage (I–V) characterizations were performed in a metal–insulator–metal (MIM) device structure (Fig. 4(a)) to understand the dielectric quality of the LiInSnO$_4$ thin film. The frequency–dependent capacitance (C–f) of the proposed LiInSnO$_4$ dielectric was studied within the frequency range of 20 Hz–20 MHz, as shown in Fig. 4(b). These data indicate that the areal capaci-

tance of LiInSnO$_4$ is ~190 nF cm^{-2} at a frequency of 50 Hz and decreases ~15% of its initial value at 500 Hz. Although it drops faster above 10^3 Hz, which is due to the mobile Li$^+$ ions that fail to contribute to its ionic polarization at higher frequencies. Since this LiInSnO$_4$ dielectric film has a high areal capacitance (≥190 nF cm^{-2}) at lower frequencies, making it suitable for TFTs with low operating voltages.[33] Moreover, the I–V characteristics (Fig. 4(c)) show that the LiInSnO$_4$ thin film has a low current density, which is due to its high compactness and a large optical band gap of 5.3 eV. Under 1 MV cm^{-1} applied electric field, the current density is ~10^{-6} A cm^{-2}, which can be low enough for fabricating a high on/off ratio TFT. Besides, the device remains stable up to an external field of 1.25 MV cm^{-1}. This high breakdown field of the LiInSnO$_4$ thin film suggests the existence of minimal pinholes with good uniformity, which is required for choosing it as a gate dielectric for a TFT.

3.4. TFT characterization

The electrical characteristics of TFTs were evaluated under dark and ambient conditions. For the output characteristics (I$_D$–V$_D$) of Device-1(Fig. 5(a)), the drain voltage (V$_D$) varied from 0 V to 2 V with a constant gate voltage (V$_G$) ranging from −0.5 V to 2 V with a step of 0.63 V (Fig. 5(b)). In the transfer characteristics (I$_D$–V$_G$) of Device-1, the gate voltage varied from −2 V to 2 V at constant drain voltage (1 V) (Fig. 5(c)). Similarly, the output characteristics of Device-2 (Fig. 5(d)) were investigated under the same applied voltages as for Device-1, as shown in Fig. 5(e). It can be noted that the accumulation mode drain current (I$_D$) of Device-2 is significantly lower (~1/20 times) than that of Device-1, which originated from the Schottky contact of the drain electrode (MoO$_3$/Ag). Besides, the transfer characteristics of Device-2 were investigated by varying V$_G$ from −1.5 to 1.5 V at a constant drain voltage of 1 V (Fig. 5(f)). The parameters such as saturation mobility (μ_{sat}), subthreshold swing (SS), and maximum number of the trap states (N_{SS}^{Max}) of the TFTs were calculated from the transfer characteristics of the devices using the following equations:[34,35]

$$\mu_{sat} = \frac{\left(\frac{\partial \sqrt{I_D}}{\partial V_G}\right)^2}{\frac{1}{2} \times \frac{W}{L} \times C} \tag{1}$$
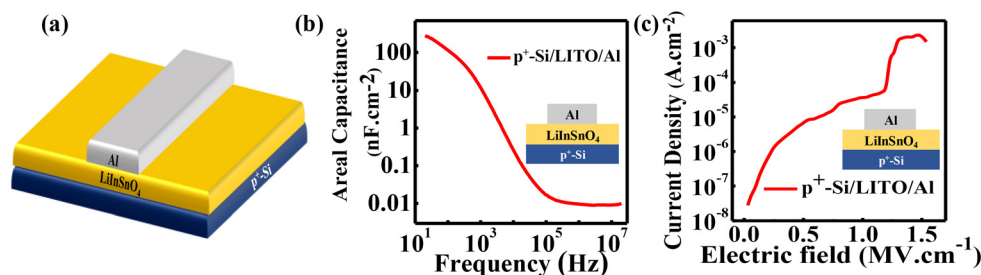
Fig. 4 (a) Schematic of the MIM device structure of p$^+$-Si/LiInSnO$_4$/Al. Electrical characterization of LiInSnO$_4$ dielectric film with MIM device. (b) Variation in capacitance with frequency and (c) variation in current density with applied field.
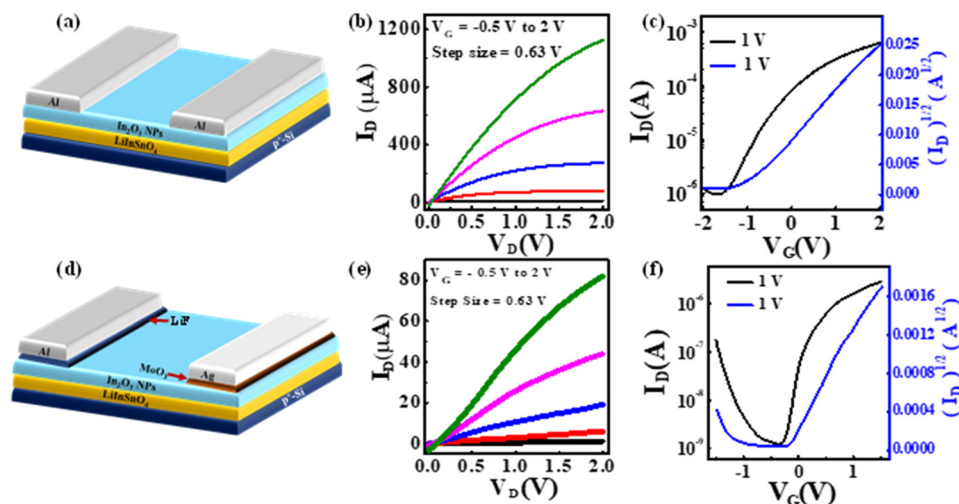
Fig. 5 (a) Schematic of Device-1 (symmetric electrodes), and its (b) output and (c) transfer characteristics. (d) Schematic of Device-2 (asymmetric electrodes), and its (e) output and (f) transfer characteristics.

$$SS = \left[\frac{\partial(\log I_D)}{\partial V_G}\right]^{-1} \quad (2)$$

$$N_{SS}^{Max} = \left[\frac{SS \times \log e}{\frac{kT}{q}} - 1\right]\frac{C}{q}. \quad (3)$$

The on/off ratios of Device-1 and Device-2 are 3.1×10^2 and 2.2×10^3, respectively. This enhancement of the on/off ratio of Device-2 is due to its Schottky contact in the drain electrode that reduces the off current of the device significantly. The effective carrier mobility (μ) of these Device-1 and Device-2 calculated using eqn (1) is 4.37 cm² V⁻¹ s⁻¹ and 0.13 cm² V⁻¹ s⁻¹, respectively. It is worth noting that the sub-threshold swing (SS) of Device-2 is 160 mV dec⁻¹, which is reduced by six times compared to Device-1 (931 mV dec⁻¹). Besides, the dielectric/semiconductor interface trap states of Device-2, calculated using eqn (3), are approximately one order lower than that of Device-1. All these parameters of Device-1 and Device-2 are summarized and compared in Table 1.

As mentioned earlier, after the electrical characterization of Device-1 and Device-2, a PbI₂ layer is over coating on both the devices. The respective output and transfer characteristics of PbI₂-coated Device-1 (Fig. 6(a)) under dark conditions are shown in Fig. 6(b) and (c), respectively, whereas these charac-

teristics for PbI₂-coated Device-2 (Fig. 6(d)) are shown in Fig. 6(e) and (f), respectively.

All electrical characterizations of these devices were performed in the same range of applied voltages as off uncoated TFTs. From Fig. 6(b), it is clear that the accumulation mode current of the PbI₂ coated Device-1 is reducing by half with respect to the uncoated device. Moreover, from Fig. 6(c), it can be noted that the off current of PbI₂-coated Device-1 also decreased by one order of magnitude with respect to the uncoated device that effectively increased the on/off ratio (~2.7 × 10³) and decreased the sub-threshold voltage of the device to 160 mV per decade. However, the effective electron mobility is reduced to 3.2 V cm⁻², which is due to the reduction of on state current. Almost similar behaviors were observed in the PbI₂-coated Device-2 as well. The summary of device parameters of PbI₂-coated Device-1 and Device-2 is given in Table 2.
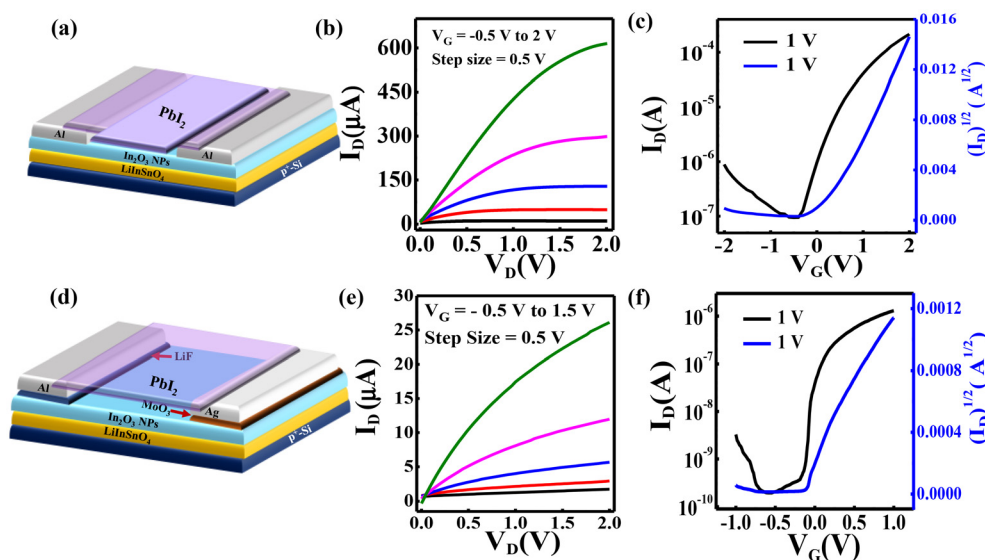
3.6. Optical response of the devices

To investigate the photoresponse of the In₂O₃ NPs thin-film transistor (TFT), a UV LED source of peak intensity at ~395 nm (Fig. SI 2(a)†) was used and the transfer characteristics of Device-1 and Device-2 are illustrated in Fig. 7(a) and (b), respectively. The In₂O₃ TFT demonstrated an observable photocurrent response under UV illumination, due to the higher energy of UV photons with respect to the band gap of the In₂O₃ NPs. The

Table 1 TFT parameters of Device-1 and Device-2 without PbI₂

Device	On–off ratio	Threshold voltage (V_{th})	Carrier mobility (cm² V⁻¹ s⁻¹)	Subthreshold swing (mV per decade)	Interface trap states density (cm⁻²)
Device-1	6.5×10^2	−1.10	4.37	682	1.24×10^{13}
Device-2	2.9×10^3	−0.19	0.13	160	2.0×10^{12}

Fig. 6 (a) Schematic of PbI$_2$-coated Device-1, and its (b) output characteristics and (c) transfer characteristics. (d) Schematic of PbI$_2$-coated Device-2, and its (e) output characteristics and (f) transfer characteristics.

Table 2 TFT parameters of Device-1 and Device-2 with an additional PbI$_2$ layer

Device	On–off ratio	Threshold voltage (V_{th})	Carrier mobility (cm^2 V^{-1} s^{-1})	Subthreshold swing (mV per decade)	Interface trap states density (cm^{-2})
Device-1 (with PbI$_2$)	2.7×10^3	−0.22	3.2	357	5.9×10^{12}
Device-2 (with PbI$_2$)	7.4×10^3	−0.14	0.14	78	3.6×10^{11}

photoresponse of the devices can be estimated in terms of the enhancement in the depletion mode drain current (off current) and the shifting in the threshold voltage. The off current and threshold voltage of Device-1 were changing by more than one order and by a difference of 2.15 V under 0.3 W m^{-2} of UV illumination, while for Device-2, these changes are more than two orders and 1.37 V, respectively. Moreover, both of the devices are illuminated with a blue LED with a peak intensity of ~445 nm (Fig. SI 2(b)†), and exhibit negligible photoresponse, as shown in Fig. SI 3(a) and SI 3(b).† The photoresponse of Device-1 was also realized through the output characteristics under UV illumination (Fig. SI 4(a)†). Therefore, it can be concluded that under UV illumination, the asymmetric S–D electrode device (Device-2) has a significantly larger variation of 'off current' and 'threshold voltage shifting' with respect to the symmetric S–D electrode device (Device-1), indicating a larger sensitivity of Device-2 under UV illumination. The shifting in the threshold voltage of the Device-1 and Device-2 is from −1.10 V to −3.2 V and −0.19 V to −1.53 V under 0.3 W m^{-2} UV illumination, respectively, as presented in Fig. 7(e).

Similar studies were performed with PbI$_2$-coated Device-1 and Device-2 by illuminating blue light, which are shown in Fig. 7(c) and (d), respectively. From these data, it is clear that the asymmetric electrode device has a larger variation of off current than that of the symmetric electrode devices. Moreover, it can be noted that the threshold voltage of PbI$_2$-

coated Device-1 shifted from −0.22 V to −1.73 V (Fig. 7(f)), whereas, in the case of the PbI$_2$-coated Device-2, this shifting is prominently lesser but is following the trend of shift towards a negative voltage axis, *i.e.* from −0.14 V to −0.39 V (Fig. 7(f)). However, the depletion mode photocurrent of PbI$_2$-coated Device-2 is seven times higher than that of PbI$_2$-coated Device-1. In Fig. SI 4(b),† the photoresponse of PbI$_2$-coated Device-1 is presented with the output characteristics under Blue light illumination.

The gate bias-dependent photosensitivity of the devices under UV and blue light illumination was calculated using eqn (4),[36] and is shown in Fig. 8. The photosensitivity of Device-1 and Device-2 under UV illumination is shown in Fig. 8(a) and (b), respectively, and it can be noted that the peak photosensitivity of Device-2 (750) is almost 18 times higher than that of Device-1 (40) at 0.3 W m^{-2} in the depletion region. The enhancement in the UV photosensitivity of Device-2 is due to the carrier selective absorption of the LiF/Al and MoO$_3$/Ag electrodes in the TFT. Similarly, the peak blue light photosensitivity of the PbI$_2$-coated Device-2 is around two times of the PbI$_2$-coated Device-1 in the flat-band region, as shown in Fig. 8(c) and (d).

$$S = \frac{I_{Ph}}{I_{dark}} = \frac{(I_{light} - I_{dark})}{I_{dark}} \qquad (4)$$
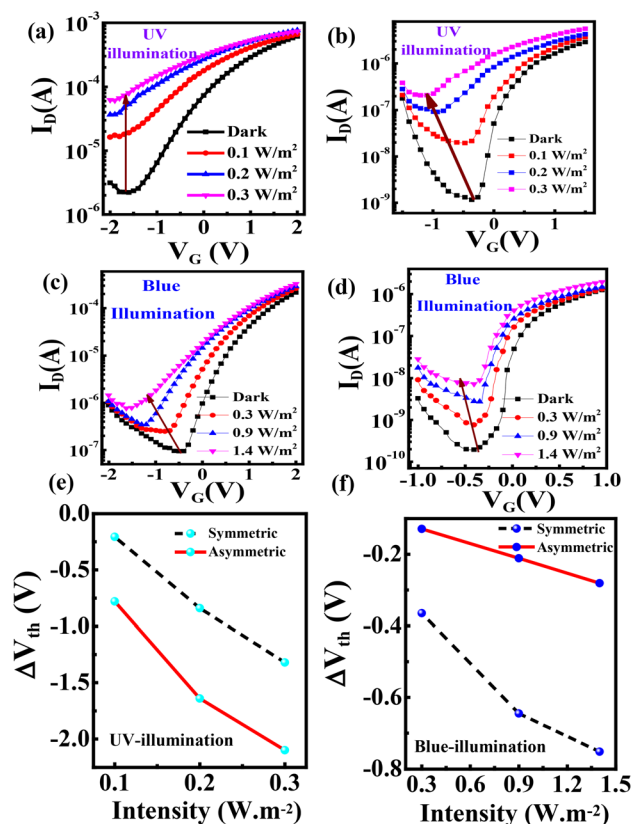
Fig. 7 Photoresponse observed in transfer characteristics under UV illumination for (a) symmetric Device-1 and (b) asymmetric Device-2, and under the blue light illumination for (c) symmetric and (d) asymmetric devices. The change in threshold voltage vs. intensity for symmetric and asymmetric electrode devices: (e) UV-illumination and (f) blue light illumination after PbI$_2$ coating.
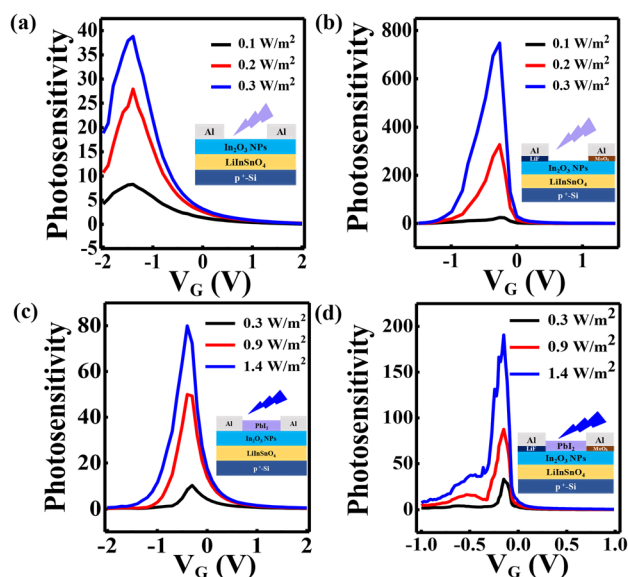

Fig. 8 Photosensitivity plot of TFTs under UV illumination with (a) symmetric electrode and (b) asymmetric electrode. Photosensitivity plot of PbI$_2$-coated TFTs under blue illumination with (c) symmetric electrode and (d) asymmetric electrode.

Moreover, the detectivity of Device-1 and Device-2 with and without the PbI$_2$-coated TFT was calculated using eqn (5) and (6):[6,37]

$$\text{Responsivity } R\,(\text{in A W}^{-1})$$
$$= \frac{I_{Ph}}{(P_{Opt} \times S)} = \frac{\text{EQE (in \%)} \times \lambda(\text{nm}) \times q}{hc \times 100} \quad (5)$$

$$\text{Detectivity } D^{\star}(\text{in Jones}) = R^{\star}\left(\sqrt{\frac{S}{(2 \times q \times I_{dark})}}\right) \quad (6)$$

where I_{Ph}, P_{opt}, S, and I_{dark} are the photocurrent, power of incident light, active area, and dark current of the device, respectively. q, I_{light}, and h are the electronic charge (1.6×10^{-19} Coulomb), device current under light conditions, and Planck's constant (6.62×10^{-34} m^2 kg s^{-1}).

The detectivity plots of TFTs under UV illumination for Device-1 and Device-2 are presented in Fig. S5(a) and S5(b),† respectively. Meanwhile, Fig. S5(c) and S5(d)† correspond to PbI$_2$-coated Device-1 and Device-2, respectively. The values of detectivity of all devices are presented in Table 3. Furthermore, symmetric electrode Device-1 exhibits a higher detectivity than that of asymmetric S–D electrode Device-2, primarily because Device-1 generates a higher photocurrent due to the formation of a good Ohmic junction at the In$_2$O$_3$ and Al interface.

3.7. Transient response of the devices

The multiple cycle transient photoresponse of Device-1 and Device-2 under UV illumination at 0.3 W m^{-2} with a gate bias of 0 V is shown in Fig. 9(a) and (b), respectively. The rise time (τ_{Rise}) and fall time (τ_{Fall}) of Device-1 are 3.1 seconds and 24.8 s, respectively. It was observed that the rise time and fall time of Device-2 are much faster than Device-1 with values of 1.9 s and 14.6 s, respectively. In addition, the transient response of Device-1 and Device-2 with a PbI$_2$ layer was measured under blue light illumination at 1.4 W m^{-2} at 0 V gate biasing, as shown in Fig. 10(a) and (b), respectively. This study gives the response time of Device-1 as rise time and fall time of 3.7 and 24 s., respectively, whereas these values are 4.6 and 40.8 s., respectively, for Device-2. A summary of the photoresponse time of the devices is given in Table 3.

3.8. External quantum efficiency of device

The external quantum efficiency (EQE) quantifies the relationship between the "quantity of generated charge carriers per incident photon" within a photodetector. The EQE data of Device-1 and Device-2 at 0 V (Black) and 2 V (Red) drain bias and 0 V gate biasing are shown in Fig. 11(a) and (b), respectively. The EQE data of both of the devices reveal its photosensitivity in the UV region only. At 2 V drain biasing, the EQE values of both the devices increase very significantly. Moreover, the values of EQE of these two devices are almost the same. However, it can be noted that the Device-2 shows a reasonable EQE at the 0-volt drain biasing (inset Fig. 11(a)), which is not observed in Device-1 (inset Fig. 11(b)). It can also be noted that no significant photocurrent is generated in the
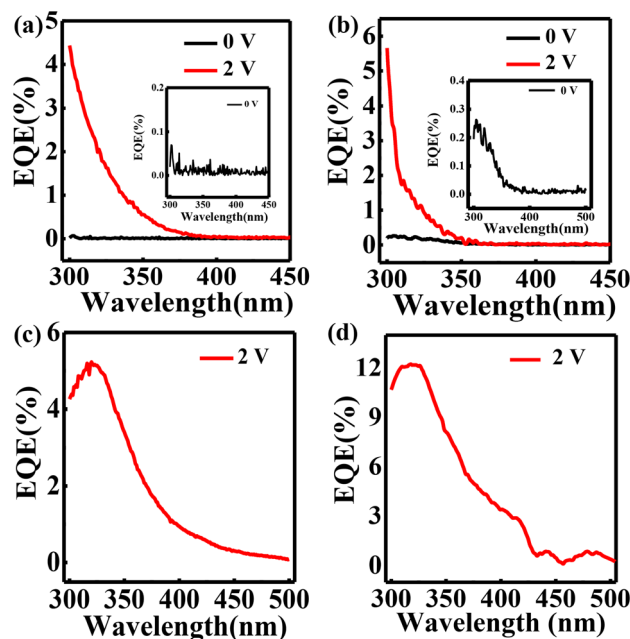
Table 3 Summary of the transient photoresponses of devices under blue light illumination

In$_2$O$_3$ TFT under UV light illumination

Device	EQE (%)	Photosensitivity at $V_G = -0.5$ V	Detectivity (Jones)	τ_{rise} (sec) UV at 0.3 W m^{-2}	τ_{fall} (sec)
Device-1	4.46	8	1.05×10^{11}	3.1	24.8
Device-2	5.69	492	4.63×10^{10}	1.9	14.6

With PbI$_2$ layer under blue light illumination

Device	EQE (%)	Photosensitivity at $V_G = -0.1$ V (depletion mode)	Detectivity (Jones)	τ_{rise} (sec) Blue at 1.4 W m^{-2}	τ_{fall} (sec)
Device-1 (with PbI$_2$)	5.29	55	4.71×10^{10}	3.7	24
Device-2 (with PbI$_2$)	12.25	152	1.9×10^{9}	4.6	40.8
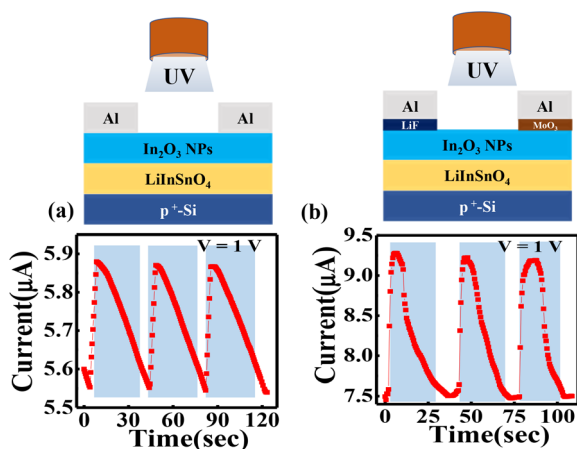
Fig. 9 Transient photoresponse of the TFT under multiple cycle UV light illumination: (a) Device-1 (with symmetric S-D electrodes) and (b) Device-2 (with asymmetric S-D electrodes).
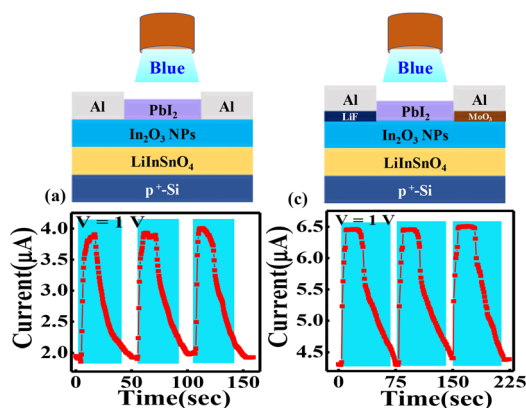
Fig. 10 Transient photoresponse of PbI$_2$-coated TFT under multiple cycle blue light illumination: (a) Device-1 (with symmetric S-D electrodes) and (b) Device-2 (with asymmetric S-D electrodes).

Fig. 11 External quantum efficiency at 0 V and 2 V without any additional PbI$_2$ layer: (a) symmetric electrode TFT and (b) asymmetric electrode TFT. External Quantum efficiency with the PbI$_2$-coated device at 2 V with (c) symmetric electrode and (d) asymmetric electrode TFTs.

region > 365 nm in both of these two devices, even after applying 2 V drain bias, depicting the visible-blind nature of the device. The EQE spectra of PbI$_2$-coated Device-1 and Device-2 at 2 V drain and 0 V gate biasing are shown in Fig. 11(c) and (d), respectively. The percentage EQE of Device-2 (~12) is higher than that of Device-1 (~5), which may be due to the additional bias originating from the asymmetric S–D electrodes of Device-2. Moreover, it is observed that with the incorporation of an additional layer of blue-sensitive PbI$_2$ material, there are notable extensions in the EQE spectra towards the visible region (450–495 nm) in the devices, confirming the blue light sensitivity of the device. Therefore, it can be concluded that these visible-blind phototransistors may become a particular color or spectrum-sensitive device based on the materials coated on top of these In$_2$O$_3$ TFTs without compromising device performance. Again photocurrent extraction in the external circuit can be improved by incorporating asym-
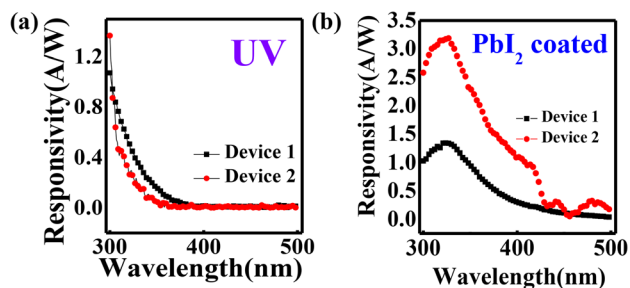
Fig. 12 Responsivity of Device-1 and Device-2: (a) without PbI$_2$ layer and (b) with PbI$_2$ layer (plotted from the EQE data).

metric work-function S-D electrodes. The responsivity data of Device-1 and Device-2 are shown in Fig. 12(a), signifying the comparable responsivity in the UV region of both the device. In contrast with PbI$_2$-coated Device-1 and Device-2, the responsivity of Device-2 exceeds that of Device-1 in the visible blue region of the electromagnetic spectra (Fig. 12(b)). Overall, the devices are showing nice photoresponse under UV as well as blue light illumination compared to the earlier reports, as presented in Table SI 1.†

3.9. Working mechanism of the device

The working principle of the photocurrent generation of these devices is explained based on the energy band alignment of the channel semiconductor with their source and drain electrodes, which is shown in Fig. 13. In the equilibrium condition, *i.e.* when the gate electrode and drain electrodes are

electrically unbiased, the energy band diagrams of Device-1 and Device-2 are shown in Fig. 13(a) and (b), respectively. It can be noted that, in the case of the symmetric electrode (Al), the potential barrier for carrier in the In$_2$O$_3$ NPs at the S and D electrodes remains the same because of the similar work function (Φ) of the Al ($\Phi_{Al} \sim 4.09$ eV).[38] Therefore, there is no driving force that allows carriers (e−) to move from the source to the drain electrode. However, in Device-2, due to substantial work function difference between the LiF/Al ($\Phi_{LiF/Al} \sim 3.79$ eV) and MoO$_3$/Ag ($\Phi_{MoO_3/Ag} \sim 4.88$ eV) electrodes,[38] it manifests band bending with a downward slope towards the drain electrode, which originated due to the thin interface layers of Al and Ag electrodes, which modulate the work function of the electrodes.[29,39] Specifically, LiF decreases the work function of the Al electrode that diminishes the barrier height (Φ_B) of electrons, dictating electron transfer from the source electrode to In$_2$O$_3$ NPs. However, the MoO$_3$ interface layer attains an optimal thickness before silver (Ag) deposition, increasing the work function of MoO$_3$/Ag beyond that of pristine Ag.[40,41] Hence, it forms a Schottky barrier for electron transport at the drain electrode and reduces the barrier potential for hole injection into the In$_2$O$_3$ NP channel simultaneously.[42] The electron transport of this Schottky junction can arise due to the thermionic emission (TE)- and thermionic field emission (TFE)-related tunneling process that effectively reduce the subthreshold swing of the device.[43] This tuning in the work function of original Al and Ag metals creates a reasonable potential difference across the (S–D) electrodes (between LiF/Al and MoO$_3$/Ag). Moreover, this potential difference across the S–D electrodes provides a driving force from the source to the
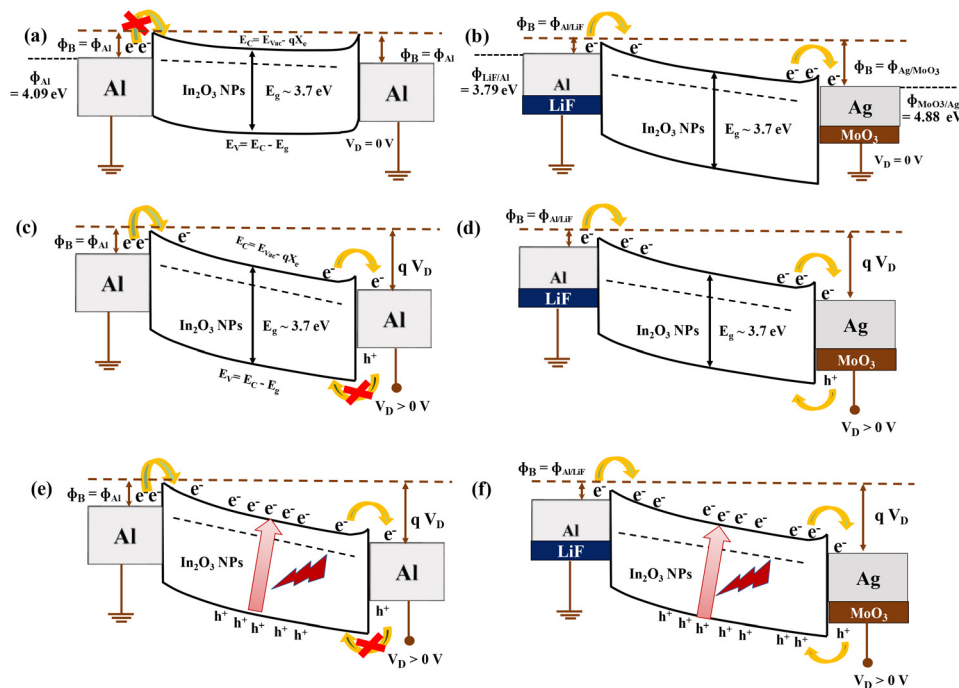

Fig. 13 Band diagram of (a) Device-1 and (b) Device-2 at equilibria with zero biasing ($V_D = 0$ V), (c) Device-1 and (d) Device-2 under electrical biasing ($V_D > 0$ V), and (e) Device-1 and (f) Device-2 under electrical ($V_D > 0$ V) and optical illumination.

drain, even at zero S–D biasing in asymmetric electrodes (Device-2), which is the origin of photocurrent generation in the EQE spectra of Device-2.[44]

Under applied positive drain biasing in the device, electrons are conducted from S to D in the In_2O_3 NP channel in both devices. However, the hole injection is strictly blocked in the Al electrode of Device-1. In contrast, there is a chance of hole conduction in Device-2, because of a lower barrier for holes at the MoO_3/Ag electrode, as shown in Fig. 13(d). The imposition of an additional positive drain bias results in an augmented barrier potential gradient between the source and drain electrodes is realized, as shown in Fig. 13(e) and (f), respectively. This heightened potential disparity prompts electron injection from the source, supplementing the population of photogenerated electrons. In both classes, electrons are drifted toward the drain electrode and concurrently, photo-generated holes move towards the source electrode under the influence of positive drain bias. This concerted effect serves to substantially reduce the rate of electron–hole recombination. Thus, Device-2 manifests an amplified photoresponse under positive drain bias with respect to Device-1. After the addition of PbI_2 layer in the channel, the absorption spectra of the transistor channel are enhanced, resulting in photo-generated carrier formation inside the PbI_2 layer due to blue light illumination. Again, photo-generated electrons can transfer to the In_2O_3 layer due to the favorable energy band and transport through this oxide channel, resulting in the blue sensitivity of the device.

4. Conclusion

In conclusion, an asymmetric work-function S–D electrode In_2O_3 NP TFT has been fabricated using an $LiInSnO_4$ thin film as a gate dielectric. This solution-processed TFT can be operated within 2 V external bias due to high areal capacitance of the $LiInSnO_4$ thin film. The on/off ratio of this asymmetric S–D electrode is ~10 times higher than that of the corresponding symmetric S–D reference device due to the elevated sheet resistance of the In_2O_3 NP channel, originating from the Schottky contact of the drain electrode. In addition, the subthreshold swing of the asymmetric S–D electrode device (Device-2) showed a depleted value compared to the symmetric electrode device (Device-1). Both Device-1 and Device-2 showed visible-blind UV sensitivity, which originated from the wide band gap of In_2O_3 NPs. Additionally, Device-2 showed enhanced photo-sensitivity with a value by 20 times under UV illumination due to the additional driving force between S–D electrodes, originating from their work-function differences. Besides, the carrier-selective charge collection to the source and drain electrodes also enhanced this effective photocurrent generation. This visible-blind UV sensitivity was further tuned to the blue region by adding PbI_2 in the channel. Therefore, this study paves the way to fabricate a phototransistor by adjusting the optical window for photosensitivity and its enhancement by choosing an additional coating or different combinations of source–drain electrodes.

Data availability

Conflicts of interest

There are no conflicts to declare.

Acknowledgements

References

1 R. Saran and R. J. Curry, *Nat. Photonics*, 2016, **10**, 81–92.
2 M. Long, P. Wang, H. Fang and W. Hu, *Adv. Funct. Mater.*, 2019, **29**, 1803807.
3 M. Ahmadi, T. Wu and B. Hu, *Adv. Mater.*, 2017, **29**, 1605242.
4 D. Yang and D. Ma, *Adv. Opt. Mater.*, 2019, **7**, 1800522.
5 S. Dahiya, S. V. Singh, U. Pandey, S. Hazra and B. N. Pal, *ACS Appl. Opt. Mater.*, 2024, **2**, 776–783.
6 H. Yoo, I. S. Lee, S. Jung, S. M. Rho, B. H. Kang and H. J. Kim, *Adv. Mater.*, 2021, **33**, 2006091.
7 N. Li, Z. Lan, L. Cai and F. Zhu, *J. Mater. Chem. C*, 2019, **7**, 3711–3729.
8 J. Guo, S. Jiang, M. Pei, Y. Xiao, B. Zhang, Q. Wang, Y. Zhu, H. Wang, J. Jie, X. Wang, Y. Shi and Y. Li, *Adv. Electron. Mater.*, 2020, **6**, 2000062.
9 S. Kim, S. Oh and J. Kim, *ACS Photonics*, 2019, **6**, 1026–1032.
10 Z. Lian, J. Wei, Z. Liu, G. Chen, H.-C. Kuo, Y. Dan, C.-C. Tu and R. Yang, *ACS Photonics*, 2024, **11**(10), 4224–4234.
11 D. Li, Y. Chen, Y. Tang, K. Liang, H. Ren, F. Li, Y. Wang, G. Liu, C. Song, L. Meng and B. Zhu, *ACS Appl. Electron. Mater.*, 2023, **5**, 578–592.
12 L. Shi and S. Nihtianov, *IEEE Sens. J.*, 2012, **12**, 2453–2459.
13 J. Zheng, H. Chong, L. Wang, S. Chen, W. Yang, G. Wei and F. Gao, *J. Mater. Chem. C*, 2020, **8**, 6072–6078.

14 Y. Yun, G. S. Han, G. N. Park, J. Kim, J. Park, D. Vidyasagar, J. Jung, W. C. Choi, Y. J. Choi, K. Heo, J. Kang, J.-S. Park, H. S. Jung and S. Lee, *Adv. Mater.*, 2022, **34**, 2270351.

15 L. Liu, C. Yang, A. Patanè, Z. Yu, F. Yan, K. Wang, H. Lu, J. Li and L. Zhao, *Nanoscale*, 2017, **9**, 8142–8148.

16 N. K. R. Nallabala, S. S. Kushvaha, S. Sangaraju and V. K. Kummara, *Mater. Sci. Semicond. Process.*, 2024, **170**, 107954.

17 N. K. R. Nallabala, S. Godavarthi, V. K. Kummara, M. K. Kesarla, C. Yuvaraj, S. Kumar, N. Ravi, G. K. Guntupalli, S. Jilani and S. P. Vattikuti, *Sol. Energy Mater. Sol. Cells*, 2021, **225**, 111033.

18 Y. Qin, S. Long, Q. He, H. Dong, G. Jian, Y. Zhang, X. Hou, P. Tan, Z. Zhang, Y. Lu, C. Shan, J. Wang, W. Hu, H. Lv, Q. Liu and M. Liu, *Adv. Electron. Mater.*, 2019, **5**, 1900389.

19 K.-J. Zhou, P.-H. Chen, Y.-Z. Zheng, M.-C. Tai, Y.-X. Wang, Y.-T. Chien, P.-J. Sun, H.-C. Huang, T.-C. Chang and S. M. Sze, *J. Mater. Chem. C*, 2022, **10**, 9192–9197.

20 B. N. Pal, P. Trottman, J. Sun and H. E. Katz, *Adv. Funct. Mater.*, 2008, **18**, 1832–1839.

21 N. K. R. Nallabala, V. R. M. Reddy, V. Singh, K. R. Bakash, S. Kumar, D. Saha, V. Mahendran, V. K. Kummara, G. K. Guntupalli and S. P. Vattikuti, *Sens. Actuators, A*, 2022, **339**, 113502.

22 B. N. Pal, B. M. Dhar, K. C. See and H. E. Katz, *Nat. Mater.*, 2009, **8**, 898–903.

23 A. Sharma, N. K. Chourasia, A. Sugathan, Y. Kumar, S. Jit, S.-W. Liu, A. Pandey, S. Biring and B. N. Pal, *J. Mater. Chem. C*, 2018, **6**, 790–798.

24 U. Pandey, N. Pal, A. Ghosh, S. Suman, S. Biring and B. N. Pal, *Nanoscale*, 2024, **16**, 8504–8513.

25 U. Pandey, N. K. Chourasia, N. Pal, S. Biring and B. N. Pal, *IEEE Trans. Electron Devices*, 2022, **69**, 1077–1082.

26 S. Yin, Y. Cheng, Y. Li, W. Liang, T. Li, J. Ma, D. Wu, Z. Shi and X. Li, *J. Mater. Sci.*, 2021, **56**, 13633–13645.

27 C. Chen, J. Moir, N. Soheilnia, B. Mahler, L. Hoch, K. Liao, V. Hoepfner, P. O'Brien, C. Qian, L. He and G. A. Ozin, *Nanoscale*, 2015, **7**, 3683–3693.

28 N. Pal, R. Chakraborty, A. Sharma, U. Pandey, V. Acharya, K. Prajapati, A. Gupta, S. Suman, P. Swaminathan,

A. K. Singh, P. K. Roy and B. N. Pal, *J. Alloys Compd.*, 2023, **960**, 170691.

29 P. K. Aich, Z. Genene, U. Pandey, A. K. Yadav, E. Wang and B. N. Pal, *ACS Photonics*, 2024, **11**, 3704–3712.

30 B. K. Yap, Z. Zhang, G. S. H. Thien, K.-Y. Chan and C. Y. Tan, *Appl. Surf. Sci. Adv.*, 2023, **16**, 100423.

31 H. Ullah, Z. H. Yamani, A. Qurashi, J. Iqbal and K. Safeen, *J. Mater. Sci.: Mater. Electron.*, 2020, **31**, 17474–17481.

32 N. Pal, B. Thakurta, R. Chakraborty, U. Pandey, V. Acharya, S. Biring, M. Pal and B. N. Pal, *J. Mater. Chem. C*, 2022, **10**, 14905–14914.

33 A. Sharma, N. K. Chourasia, A. Sugathan, Y. Kumar, S. Jit, S.-W. Liu, A. Pandey, S. Biring and B. N. Pal, *J. Mater. Chem. C*, 2018, **6**, 790–798.

34 R. Chen and L. Lan, *Nanotechnology*, 2019, **30**, 312001.

35 R. Shyam, P. K. Aich, U. Pandey, B. N. Pal and R. Prakash, *IEEE Sens. J.*, 2024, **24**(20), 32004–32010.

36 R. Shyam, T. Manaka and R. Prakash, *J. Mater. Chem. C*, 2024, **12**, 18514–18525.

37 S. Suman, U. Pandey, N. Pal, P. Swaminathan and B. N. Pal, *ACS Photonics*, 2023, **11**, 93–101.

38 S. Dahiya, U. Pandey, S. Hazra, R. Chakraborty, S. Pramanik, P. P. Maurya and B. N. Pal, *Adv. Mater. Technol.*, 2025, **10**(7), 2401532.

39 T. Brown, R. Friend, I. Millard, D. Lacey, J. Burroughes and F. Cacialli, *Appl. Phys. Lett.*, 2000, **77**, 3096–3098.

40 U. Pandey, A. K. Yadav, N. Pal, P. K. Aich and B. N. Pal, *J. Mater. Chem. C*, 2023, **11**, 15276–15287.

41 S. Dahiya, S. Hazra, U. Pandey, S. Pramanik, P. Dahiya, S. V. Singh, N. Kumari and B. N. Pal, *Opt. Mater.*, 2024, **157**, 116182.

42 A. V. Polotai, T.-H. Jeong, G.-Y. Yang, E. C. Dickey, C. A. Randall, P. Pinceloup and A. S. Gurav, *J. Electroceram.*, 2009, **23**, 6–12.

43 S. Lee and A. Nathan, *Science*, 2016, **354**, 302–304.

44 N. K. R. Nallabala, S. P. Vattikuti, V. Verma, V. Singh, S. Alhammadi, V. K. Kummara, V. Manjunath, M. Dhanalakshmi and V. R. M. Reddy, *Mater. Sci. Semicond. Process.*, 2022, **138**, 106297.